Journal of Power Sources 245 (2014) 712–720

Contents lists available at SciVerse ScienceDirect

Journal of Power Sources

journal homepage: www.elsevier.com/locate/jpowsour

Analytical assessment of the thermal behavior of nickel–metal hydride batteries during fast charging

Peyman Taheri, Maryam Yazdanpour, Majid Bahrami*

Laboratory for Alternative Energy Conversion (LAEC), Mechatronic Systems Engineering, School of Engineering Science, Simon Fraser University, Surrey, BC V3T 0A3, Canada

HIGHLIGHTS

- An analytical distributed thermal model is proposed to investigate transient thermal behavior of NiMH batteries.
- The thermal model uses integral transformation technique with minimum computational effort.
- The model is successfully validated against numerical and experimental data.
- The new index of charging efficiency is defined for charging processes.

ARTICLE INFO

Article history:
Received 23 February 2013
Received in revised form
13 June 2013
Accepted 14 June 2013
Available online 25 June 2013

Keywords:
Battery thermal management
Battery thermal model
Fast charging of batteries
Charging efficiency
Integral-transformation technique
Nickel–metal hydride battery

ABSTRACT

A novel distributed transient thermal model is proposed to investigate the thermal behavior of nickel–metal hydride (NiMH) batteries under fast-charging processes at constant currents. Based on the method of integral transformation, a series-form solution for the temperature field inside the battery core is obtained that takes account for orthotropic heat conduction, transient heat generation, and convective heat dissipation at surfaces of the battery. The accuracy of the developed theoretical model is confirmed through comparisons with numerical and experimental data for a sample 30 ampere-hour NiMH battery. The comparisons show that even the first term of the series solution fairly predicts the temperature field with the modest numerical cost. The thermal model is also employed to define an efficiency for charging processes. Our calculations confirm that the charging efficiency decreases as the charging current increases.

1. Introduction

Since 1990, when the first nickel–metal hydride (NiMH) batteries commercialized in Japan [1], they have been adapted to a wide range of applications from handheld electronics to hybrid and electric vehicles [2,3]. Recently, lithium-ion (Li-ion) batteries are realized as the new competent for NiMH cells, thanks to their outstanding energy density, minimal memory effect and low self discharge rate. Nonetheless, NiMH cells are expected to sustain their position in the market due to their environmental friendliness and better thermal stability [4].

Despite technological achievements in chemistry optimization, electrodes design, and fabrication of advanced secondary batteries, including NiMH cells, their large-scale application has not reached its full potential. This shortcoming is associated with the fact that cycle life, charge intake and power delivery characteristics of batteries strongly depends on temperature and heat generation during charging/discharging processes. Accordingly, thermal management of power batteries is an important and timely issue owing to its crucial role in battery safety, performance, and longevity. To highlight the importance of operational temperature in batteries it suffices to mention that high temperatures in NiMH cells lead to pressure buildup as a result of gas accumulation from the side reactions [5,6], which in turn may cause structural failure and electrolyte leakage (capacity fade) [7]. For NiMH batteries, it is evident that thermal issues are more pronounced during charging processes rather than discharging [4,8].

* Corresponding author.
E-mail addresses: ptaherib@sfu.ca (P. Taheri), myazdanp@sfu.ca (M. Yazdanpour), mbahrami@sfu.ca (M. Bahrami).

0378-7753/$ – see front matter © 2013 Elsevier B.V. All rights reserved.
http://dx.doi.org/10.1016/j.jpowsour.2013.06.086

With the fast-paced development of computational methods and computer technology, thermo-electrochemical modeling of batteries has become an essential approach in their design and optimization. For nickel based batteries, several rigorous mathematical models at electrode level have been developed, for examples see Refs. [9–17]. Such models are suitable to i) investigate the underlying physicochemical mechanisms, ii) optimize the effects of electrode designs (electrode thickness and particle size) on scale-up battery system, and iii) predict battery behavior in different operating conditions. However, for large-scale batteries detailed thermo-electrochemical simulations are not plausible computationally; instead, standalone thermal models or electro-thermal models with focus on thermal response of the battery under different operating conditions are favorable.

The main challenge in thermal modeling of NiMH batteries is the evaluation of heat generation rate during charge/discharge processes. A common practice is to use direct or indirect calorimetry techniques for *in-situ* measurement of the battery heat generation and its corresponding temperature [7,18]. An alternative approach is to approximate the heat generation rate in a battery from its electrical performance, and solve the energy balance equation for temperature [19]. In the present paper the latter approach is employed to investigate thermal response of a NiMH battery during rapid-charging processes.

To the authors' best knowledge, multi-dimensional thermal models for NiMH batteries are all based on numerical approaches and are mostly adapted for cylindrical cells. Therefore, lack of a "theoretical" distributed model is apparent in the literature. From the computational point of view, analytical solutions are highly on demand because they are continuous in the independent variables, and show explicitly how the parameters of the system are involved. Furthermore, analytical solutions give much insight into a system, which is one of the primary objectives of modeling. Accordingly, in the present study, a three-dimensional "analytical" thermal model which was originally developed for Li-ion batteries [20], is adapted to describe the transient thermal behavior of NiMH batteries. The model is employed to describe the evolution of unsteady temperature field in a prismatic 30 A h NiMH battery under fast-charging processes with constant-currents, and the results are compared to those of accurate numerical simulations and experimental data available in the literature [21]. The comparisons show favorable agreement with both numerical and experimental data.

The proposed model provides a series-form solution for the energy equation with orthotropic thermal conductivities, and takes account for unsteady heat generation rate, the effects of side-reactions on the heat generation rate, and convective heat transfer at boundaries. Through comparisons, it is shown the analytical series-form solution rapidly converges to the numerical solution and fairly matches with the experimental measurements. Indeed, its leading terms provide a simple yet accurate approximation of the battery thermal behavior with modest numerical effort.

In the following sections, details of the theoretical thermal model are explained and its implementation to a sample NiMH cell is demonstrated. Evolution of the temperature field inside the battery core is discussed for two charging rates, while natural- and forced-convective cooling conditions at its case surfaces are assumed.

Finally, it is worth mentioning that although the method is implemented for charging processes of a NiMH battery, its generality allows to use it for thermal characterization of batteries with different chemistries during discharge processes as well [20].

2. Thermal model

We consider a 30 A h prismatic NiMH cell (NEXcell battery, USA), for which experimental and numerical temperature data during rapid-charging processes are reported in Ref. [21]. Conventionally, Constant Current–Constant Voltage (CC–CV) protocols are recommended to charge batteries up to their full capacity. However, in a rapid-charging, the time taking Constant Voltage step is excluded.

As shown in Fig. 1a, the dimensions of the battery are $20 \times 110 \times 90$ mm. In our analysis we divide the battery into two regions: the core region, and the case region. The battery core ($L_1 \times L_2 \times L_3 = 19 \times 109 \times 89$ mm), shown in Fig. 1b, includes a plurality of positive nickel electrodes, negative metal hydride electrodes, and nylon separator sheets. All components of the battery core are encased in a stainless steel container, i.e., the case region, with the thickness of 0.5 mm. The electrodes that accommodate active materials required in the battery chemistry and the separator sheets that serve as ion-exchange membranes have porous structures, and their pores are filled with a concentrated KOH solution as the electrolyte. For the considered battery the total thickness, porosity, and thermal conductivity of battery layers and electrolyte liquid are listed in Table 1, borrowed from Ref. [21].

During the battery operation, heat is generated non-uniformly within the battery core. The transient temperature field inside the battery core is described by a three-dimensional energy balance equation which only includes conduction terms,

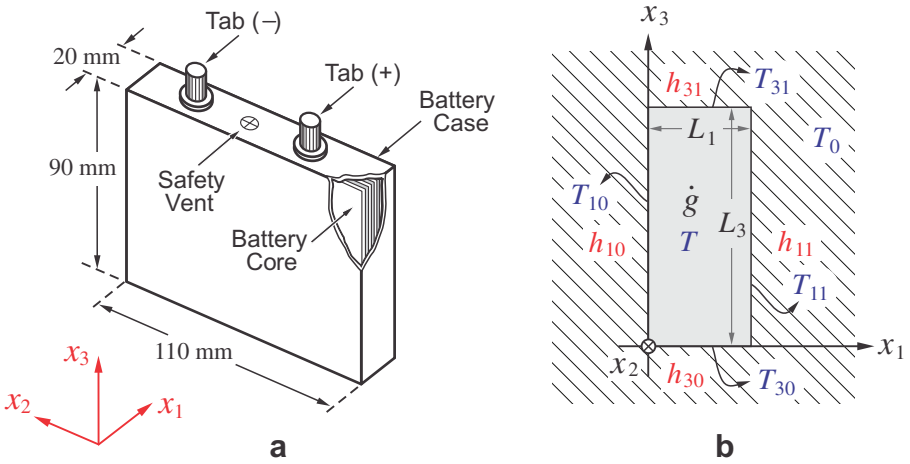

Fig. 1. a) Schematic and dimensions of the sample 30 A h NiMH battery. b) Two-dimensional schematic of the battery core in x_1–x_3 plane with internal heat generation $\dot{g}$, and convective heat dissipation at boundaries. The ambient temperature is denoted by T_0.

Table 1
Total thickness, porosity, and thermal conductivity of battery components [21].

Material/layer	Thickness (total)	Porosity	Thermal conductivity
	ℓ [mm]	ε	κ [W m^{-1} K^{-1}]
Negative electrode	5.40	0.27	1.16
Positive electrode	7.37	0.22	1.14
Separator sheet	6.23	0.74	0.22
Electrolyte	–	–	0.57
Case	0.50	–	16

$$\rho c_p \frac{\partial T}{\partial t} = \kappa_1 \frac{\partial^2 T}{\partial x_1^2} + \kappa_2 \frac{\partial^2 T}{\partial x_2^2} + \kappa_3 \frac{\partial^2 T}{\partial x_3^2} + \dot{g}, \quad 0 \le x_1 \le L_1, \quad 0 \le x_2 \le L_2, \quad 0 \le x_3 \le L_3, \quad t > 0, \tag{1}$$

in which t is time, and $\boldsymbol{x} = \{x_1, x_2, x_3\}$ represents the components of the position vector in Cartesian coordinate system. The functions $T(\boldsymbol{x},t)$ and $\dot{g}(\boldsymbol{x},t)$ denote the temperature and volumetric heat generation rate inside the battery core, respectively (see Fig. 1b). The density ρ, specific heat c_p, and orthotropic thermal conductivities κ_i are the thermophysical parameters for the core region, for which the values are listed in Table 2.

To evaluate thermal conductivities of porous electrodes and separators, it is assumed that their pores are fully filled with the electrolyte liquid, and their thermal conductivities are approximated as [22],

$$\kappa = \kappa_s(1-\varepsilon) + \kappa_f \varepsilon, \tag{2}$$

where ε is the porosity of each layer, listed in Table 1. The subscripts 's' and 'f' correspond to solid structural materials (electrodes and separators), and liquid filler (electrolyte), respectively.

In order to avoid complexities associated with heat transfer in multi-material multi-layered structure of the battery core, it is common to define effective thermal conductivities for the whole battery core. For this, the concept of equivalent thermal resistance network can be employed to define effective thermal conductivity in different directions. Based on Fig. 1a, there are series thermal resistors in x_1-direction and parallel thermal resistors in x_2- and x_3-directions. Therefore, by using the data from Table 1, through-plane and in-plane thermal conductivities are evaluated as [23],

$$\kappa_1 = \frac{\sum_N \ell_N}{\sum_N (\ell_N/\kappa_N)} = \frac{\ell_p + \ell_n + \ell_m}{\ell_p/\kappa_p + \ell_n/\kappa_n + \ell_m/\kappa_m} = 0.74 \left[\mathrm{W\ m^{-1}\ K^{-1}}\right], \tag{3a}$$

$$\kappa_2 = \kappa_3 = \frac{\sum_N \ell_N \kappa_N}{\sum_N \ell_N} = \frac{\ell_p\kappa_p + \ell_n\kappa_n + \ell_m\kappa_m}{\ell_p + \ell_n + \ell_m} = 0.84 \left[\mathrm{W\,m^{-1}\,K^{-1}}\right], \tag{3b}$$

where ℓ is the (total) thickness of each porous layer in x_1-direction (see Fig. 1a), κ is its averaged thermal conductivity obtained from Eq. (2), and N is the number of different layers (negative electrode, positive electrode and separator). The subscripts 'p', 'n', and 'm' correspond to positive electrode, negative electrode, and membrane (separator), respectively.

Convection thermal boundary conditions are applied at the surfaces of the battery case,

$$-\kappa_i \frac{\partial T}{\partial x_i} + \left[\frac{\ell_{case}}{\kappa_{case}} + \frac{1}{h_{i0,case}}\right]^{-1} (T_{i0} - T_0) = 0, \quad \text{at } x_i = 0\ (i = 1,2,3), \tag{4a}$$

$$+\kappa_i \frac{\partial T}{\partial x_i} + \left[\frac{\ell_{case}}{\kappa_{case}} + \frac{1}{h_{i1,case}}\right]^{-1} (T_{i1} - T_0) = 0, \quad \text{at } x_i = L_i\ (i = 1,2,3), \tag{4b}$$

where $h_{ij,case}$ are the convective heat transfer coefficients at different surfaces of the case, and T_{ij} are the corresponding surface temperatures. The index i represents the direction of the normal vector on a boundary surface, while $j = 0$ and $j = 1$ denote surfaces at $x_i = 0$ and $x_i = L_i$, respectively (see Fig. 1b). The thickness of the battery case and its thermal conductivity (Table 1) are denoted by ℓ_{case} and κ_{case}. The environment temperature T_0 is assumed to be a constant.

The convective heat transfer coefficients at the surface of the battery core are h_{ij},

$$h_{ij} = \left[\frac{\ell_{case}}{\kappa_{case}} + \frac{1}{h_{ij,case}}\right]^{-1}, \ (i = 1,2,3; j = 0,1). \tag{5}$$

The initial temperature of the core is the same as environment temperature T_0,

$$T = T_0, \quad \text{at } t = 0. \tag{6}$$

In this study, we consider constant ambient temperatures; however, the method allows definition of ambient temperatures as a function of both space and time [24,25].

Determination of heat generation rate $\dot{g}(\boldsymbol{x},t)$ is one of the most challenging tasks in thermal modeling of battery systems. Heat generation inside batteries is a complex process that requires understanding of how the rates of electrochemical reactions change with time and temperature and how the current is distributed within battery electrodes [26].

The rate of heat generation inside the battery can be approximated from the well-known energy balance analysis proposed by Bernardi et al. [27],

$$\dot{g} = \pm \frac{I}{\mathscr{V}} \left[(V - V_{oc}) + T\frac{dV_{oc}}{dT}\right], \tag{7}$$

with positive and negative signs for charge and discharge processes, respectively. The parameters I and V denote operational current and voltage of the battery, and $\mathscr{V}$ is the battery core volume. Open circuit voltage (OCV) of the battery, also known as equilibrium potential, is denoted by V_{oc}. The first term, $I(V - V_{oc})/\mathscr{V}$, is the irreversible heat and the second term, $IT(dV_{oc}/dT)/\mathscr{V}$, is the reversible heat. The Reversible and irreversible heats correspond to different mechanism of heat generation inside the battery.

Table 2
Thermophysical properties and the entropic heat generation coefficient for the battery core [21].

Parameter	κ_1 [W m^{-1} K^{-1}]	κ_2 [W m^{-1} K^{-1}]	κ_3 [W m^{-1} K^{-1}]	ρ [kg m^{-3}]	c_p [J kg^{-1} K^{-1}]	$T\,(dV_{oc}/dT)$ [V]
Values	0.74	0.84	0.84	3520	3200	0.023

While the irreversible heat, due to battery overpotential, is always positive, i.e., the heat leading to temperature rise, the sign of the reversible heat, caused by the entropy change in electrochemical reactions, may be positive or negative based on the process (charging or discharging) and also the battery chemistry.

For convenience in comparison of different charging processes, we use SoC (state-of-charge) instead of time. Given an initial SoC at $t = 0$ and assuming 100% coulombic efficiency, SoC (in %) can be related to the charging time t (s) via,

$$\mathrm{SoC}(t) = \mathrm{SoC}(0) + \frac{1}{3600Q}\int_0^t I(t)\mathrm{d}t, \tag{8}$$

where Q is the nominal battery capacity in ampere-hour. According to Eq. (8), for a fully discharged battery which undergoes constant current charging processes, SoC and time are related linearly,

$$\mathrm{SoC}(t) = \frac{I}{3600Q}t. \tag{9}$$

It is important to point out that SoC is conventionally defined as the fraction of battery capacity Q stored during a charge process, however, in our analysis and in the presented plots SoC serves as a dimensionless index for charging time.

During charging process of a NiMH battery, the primary charging reactions (main redox reactions) and side reactions both occur inside the battery. The main charging reactions in the positive (nickel) and negative (metal hydride) electrodes are,

$$\text{Positive}: \mathrm{Ni(OH)_2} + \mathrm{OH^-} \rightarrow \mathrm{NiOOH} + \mathrm{H_2O} + \mathrm{e^-} \tag{10a}$$

$$\text{Negative}: \mathrm{H_2O} + \mathrm{M} + \mathrm{e^-} \rightarrow \mathrm{OH^-} + \mathrm{MH} \tag{10b}$$

The side reactions involve oxygen reduction at the positive electrode and oxygen evolution at the negative electrode,

$$\text{Positive}: \frac{1}{2}\mathrm{O_2} + \mathrm{H_2O} + 2\mathrm{e^-} \rightarrow 2\mathrm{OH^-} \tag{11a}$$

$$\text{Negative}: 2\mathrm{OH^-} \rightarrow \frac{1}{2}\mathrm{O_2} + \mathrm{H_2O} + 2\mathrm{e^-} \tag{11b}$$

while these two side reactions are coupled by an internal oxygen transport from the negative electrode to the positive electrode [16].

At low values of SoC, the primary charging reaction is dominant at the negative electrode and the rate of oxygen evolution is suppressed. However, at high values of SoC, particularly during the overcharge period, oxygen gas evolves in higher rates since at high potentials the aqueous electrolyte is thermodynamically unstable. This leads to higher rates of internal oxygen cycle reaction, and consequently, the open-circuit voltage decreases to zero [21].

From heat generation point of view, at high SoC the heat generation rate increases rapidly owing to the oxygen recombination heat at the positive electrode.

To account for the effects of side reactions in battery heat generation, the total charging current I is split into the current of charging reaction I_1, and the current of internal oxygen cycle reaction (side reactions) I_2. The linear current splitting scheme which is used in our analysis is shown in Fig. 2, for which side reactions initiate at SoC = 75%. In account for Fig. 2, for the considered NiMH battery Eq. (7) becomes,

$$\dot{g} = \frac{1}{\mathscr{V}}\left(IV - I_1 V_{\mathrm{oc}} + I_2 T\frac{\mathrm{d}V_{\mathrm{oc}}}{\mathrm{d}T}\right), \tag{12}$$

where $I = I_1 + I_2$.

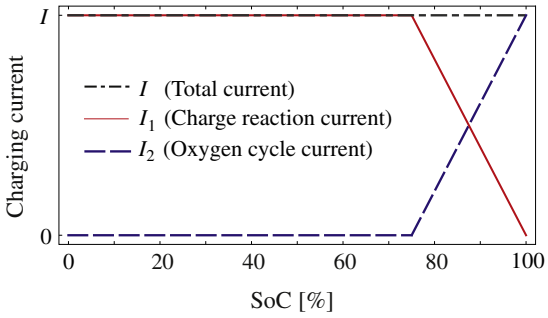

Fig. 2. Schematic of the linear current splitting model for the sample NiMH battery [21]. When state-of-charge (SoC) exceeds ~75%, side reactions become dominant. The total current of the battery I is the summation of the main charging reaction current I_1 and the oxygen cycling current I_2.

The SoC corresponding to the onset of side reactions is a battery characteristic, but it also depends on the temperature. For example in some cylindrical NiMH batteries, side reactions become dominant at SoC > 90% and their effects are more pronounced when the batteries are overcharged [18].

Adiabatic calorimetry of the battery during a constant current charging process allows to relate the rate of heat generation inside the battery to its temperature rise. When battery temperature increases, the chamber of an accelerating rate calorimeter (ARC) can follow the temperature of the battery. Thus, no heat exchange happens between the battery and the chamber, and all the heat generated inside the battery will be used for its temperature rise, i.e.,

$$\dot{g} = \frac{I}{\mathscr{V}}\left[(V - V_{\mathrm{oc}}) + T\frac{\mathrm{d}V_{\mathrm{oc}}}{\mathrm{d}T}\right] = \rho c_p \frac{\mathrm{d}T}{\mathrm{d}t}, \tag{13}$$

as long as the oxygen cycle reaction is not started; that for this case is SoC < 75%.

By replacing $V - V_{\mathrm{oc}} = IR_z$ in Eq. (13) the following relation can be obtained [28],

$$\frac{R_z}{mc_p}I + \frac{T}{mc_p}\frac{\mathrm{d}V_{\mathrm{oc}}}{\mathrm{d}T} = \frac{1}{I}\frac{\mathrm{d}T}{\mathrm{d}t}, \tag{14}$$

where R_z is the apparent DC cell resistance. Based on Eq. (14), for a given charging current I, if $(1/I)(dT/dt)$ is plotted against I, an approximately straight line is obtained with the slope R_z/mc_p and the intercept $(T/mc_p)(dV_{\mathrm{oc}}/dT)$.

For different charging currents, values of $(1/I)(dT/dt)$ for the considered battery are reported in Ref. [21]. Since the mass of battery is known, the values for c_p and $T(dV_{\mathrm{oc}}/dT)$ are obtained, as listed in Table 2. Note that from the calorimetry measurement, the total heat capacity of the battery (core and case) is evaluated as 2788 [J kg^{-1} K^{-1}], but the heat capacity of the core is used in our calculations, which is approximated as $c_p = 3200$ [J kg^{-1} K^{-1}].

3. Analytical solution

Equation (1) is a linear energy balance equation for which analytical solution is accessible. The key assumption in derivation of the linear energy equation is that the thermophysical properties are not temperature dependent. This assumption holds for batteries with a narrow range for temperature change during their operation. Furthermore, due to the porosity of battery components, the motion of the electrolyte is neglected, thus the convective terms do not appear in the governing energy equation.

To generalize the analysis, dimensionless quantities can be introduced. We use the largest value of κ_i/L_i^2, which happens to be in x_1 direction, to scale the governing equations, i.e., Eqs. (1), (4), (6) and (12).

The dimensionless coordinate system ξ_i, and dimensionless time τ are defined as,

$$\xi_i = \frac{x_i}{L_i}\ (i = 1,2,3),\quad \tau = \frac{\kappa_1/L_1^2}{\rho c_p/t}. \tag{15}$$

Rewriting the initial-boundary-value problem, i.e., Eqs. (1), (4), and (6), in terms of the dimensionless position and time gives,

$$\frac{\partial\theta}{\partial\tau} = \frac{\partial^2\theta}{\partial\xi_1^2} + K_2\frac{\partial^2\theta}{\partial\xi_2^2} + K_3\frac{\partial^2\theta}{\partial\xi_3^2} + \dot{G},\quad 0 \le \xi_1 \le 1,\quad 0 \le \xi_2 \le 1,$$
$$0 \le \xi_3 \le 1,\quad \tau > 0, \tag{16}$$

with the boundary conditions,

$$-\frac{\partial\theta}{\partial\xi_i} + \mathrm{Bi}_{i0}\theta_{i0} = 0,\quad \text{at } \xi_i = 0\ (i = 1,2,3), \tag{17a}$$

$$+\frac{\partial\theta}{\partial\xi_i} + \mathrm{Bi}_{i1}\theta_{i1} = 0,\quad \text{at } \xi_i = 1\ (i = 1,2,3), \tag{17b}$$

and the initial condition,

$$\theta = 0,\quad \text{at } \tau = 0. \tag{18}$$

In Eq. (16), K_i are the dimensionless thermal conductivities, and in the transformed boundary conditions [cf. Eq. (17)] Bi_{ij} are Biot numbers,

$$K_i = \frac{\kappa_i/L_i^2}{\kappa_1/L_1^2}\ (i = 1,2,3),\quad \mathrm{Bi}_{ij} = \frac{h_{ij}L_i}{\kappa_i}\ (i = 1,2,3; j = 0,1), \tag{19}$$

The temperature rise inside the battery core is denoted by θ, and the temperature rise on its boundaries are θ_{ij},

$$\theta = T - T_0,\quad \theta_{ij} = T_{ij} - T_0. \tag{20}$$

The source for temperature rise $\dot{G}$ (in temperature unit) is,

$$\dot{G} = \frac{\dot{g}}{\kappa_1/L_1^2} = \dot{G}_{\mathrm{irrev}} + \dot{G}_{\mathrm{rev}}, \tag{21a}$$

with,

$$\dot{G}_{\mathrm{irrev}} = \frac{1/\mathscr{V}}{\kappa_1/L_1^2}(IV - I_1V_{\mathrm{oc}}),\quad \dot{G}_{\mathrm{rev}} = \frac{1/\mathscr{V}}{\kappa_1/L_1^2}(0.023I_2). \tag{21b}$$

During the battery operation both $\dot{G}_{\mathrm{irrev}}$ and $\dot{G}_{\mathrm{rev}}$ vary with SoC (or time), since I_1, I_2, V, and V_{oc} are functions of SoC (or time). The charge reaction current, I_1, contributes only to the irreversible heat, while the oxygen cycle current, I_2, contributes to both reversible and irreversible heats.

Here, the product of T and dV_{oc}/dT is a constant obtained from calorimetry; however, when variation of V_{oc} with respect to temperature is known, a different strategy for treating the reversible heat generation must be employed; see Ref. [20] for details.

The transformed system [cf. Eqs. (16)–(18)] that describes temperature rise with respect to the dimensionless space and time, is solved analytically using a finite-integral transform technique, as described below.

The triple integral transformation and the inversion formula for temperature function are defined as [24],

$$\overline{\theta}(\lambda_{1l},\lambda_{2m},\lambda_{3n},\tau) = \int_{\xi_1'=0}^{1}\int_{\xi_2'=0}^{1}\int_{\xi_3'=0}^{1}\psi(\lambda_{1l},\xi_1')\cdot\psi(\lambda_{2m},\xi_2')\cdot\psi(\lambda_{3n},\xi_3')\cdot\theta(\xi_1',\xi_2',\xi_3',\tau)\cdot\mathrm{d}\xi_1'\cdot\mathrm{d}\xi_2'\cdot\mathrm{d}\xi_3', \tag{22}$$

and,

$$\theta(\xi_1,\xi_2,\xi_3,\tau) = \sum_{l=1}^{\infty}\sum_{m=1}^{\infty}\sum_{n=1}^{\infty}\psi(\lambda_{1l},\xi_1)\cdot\psi(\lambda_{2m},\xi_2)\cdot\psi(\lambda_{3n},\xi_3)\cdot\overline{\theta}(\lambda_{1l},\lambda_{2m},\lambda_{3n},\tau). \tag{23}$$

The functions $\psi(\lambda_{1l},\xi_1)$, $\psi(\lambda_{2m},\xi_2)$, and $\psi(\lambda_{3n},\xi_3)$ are the transformation kernels (normalized eigenfunctions) in ξ_1, ξ_2, and ξ_3 directions,

$$\psi(\lambda_i,\xi_i) = \frac{\phi(\lambda_i,\xi_i)}{\alpha_i^{1/2}}\ (i = 1,2,3), \tag{24}$$

and $\phi(\lambda_i,\xi_i)$ are the eigenfunctions,

$$\phi(\lambda_i,\xi_i) = \cos(\lambda_i\xi_i) + \frac{\mathrm{Bi}_{i0}}{\lambda_i}\sin(\lambda_i\xi_i)\ (i = 1,2,3), \tag{25}$$

The eigenfunctions are solutions of the following Sturm–Liouville system corresponding to Eqs. (16) and (17),

$$\frac{\mathrm{d}^2\phi}{\mathrm{d}\xi_i^2} + \lambda_i^2\phi = 0\ (i = 1,2,3), \tag{26a}$$

$$-\frac{\mathrm{d}\phi}{\mathrm{d}\xi_i} + \mathrm{Bi}_{i0}\phi = 0,\quad \text{at } \xi_i = 0\ (i = 1,2,3), \tag{26b}$$

$$+\frac{\mathrm{d}\phi}{\mathrm{d}\xi_i} + \mathrm{Bi}_{i1}\phi = 0,\quad \text{at } \xi_i = 1\ (i = 1,2,3), \tag{26c}$$

In Eqs. (24)–(26), λ_i denote an infinite list of eigenvalues in ξ_i direction. In Eqs. (22) and (23) components of λ_i in ξ_1, ξ_2, and ξ_3 directions are denoted by λ_{1l}, λ_{2m}, and λ_{3n}, respectively. The subscripts l, m, and n are the indices for the list components. The eigenvalues in each direction are positive roots of the following transcendental equation [24],

$$\tan\lambda = \frac{\lambda(\mathrm{Bi}_{i0} + \mathrm{Bi}_{i1})}{\lambda^2 - \mathrm{Bi}_{i0}\mathrm{Bi}_{i1}},\ (i = 1,2,3). \tag{27}$$

Eigenvalues normalization factors α_i, which appear in Eq. (24), are obtained as [24],

$$\alpha_i = \frac{1}{2}\left[\frac{\lambda_i^2 + \mathrm{Bi}_{i0}^2}{\lambda_i^2}\left(1 + \frac{\mathrm{Bi}_{i1}}{\lambda_i^2 + \mathrm{Bi}_{i1}^2}\right) + \frac{\mathrm{Bi}_{i0}}{\lambda_i^2}\right],\ (i = 1,2,3). \tag{28}$$

The integral transform of Eq. (16), according to transformation (22), yields the following ordinary differential equation for $\overline{\theta}$,

$$\frac{\mathrm{d}\overline{\theta}}{\mathrm{d}\tau} + \Delta_{lmn}\overline{\theta} = \overline{\dot{G}},\quad \text{with } \overline{\theta}(\tau) = 0 \text{ at } \tau = 0. \tag{29a}$$

in which,

$$\Delta_{lmn} = \lambda_{1l}^2 + K_2\lambda_{2m}^2 + K_3\lambda_{3n}^2. \tag{29b}$$

Quantities with a bar refer to transformed quantities as given by Eq. (22), i.e.,

$$\overline{\dot{G}}(\lambda_{1l},\lambda_{2m},\lambda_{3n},\tau) = \int_{\xi_1'=0}^{1}\int_{\xi_2'=0}^{1}\int_{\xi_3'=0}^{1}\psi(\lambda_{1l},\xi_1')\cdot\psi(\lambda_{2m},\xi_2')\cdot\psi(\lambda_{3n},\xi_3')\cdot\dot{G}(\tau)\cdot d\xi_1'\cdot d\xi_2'\cdot d\xi_3', \quad (29c)$$

Equation (29a) is a first-order, linear, and inhomogeneous ODE with a constant coefficient Δ_{lmn}. Its solution $\overline{\theta}(\lambda_{1l},\lambda_{2m},\lambda_{3n},\tau)$ can be obtained as,

$$\overline{\theta} = \exp(-\Delta_{lmn}\tau)\left[\int_{\tau}\overline{\dot{G}}(\tau)\exp(\Delta_{lmn}\tau)d\tau + \mathscr{C}\right], \quad (30)$$

for which the corresponding integrating constant $\mathscr{C}$ must be evaluated from the given initial condition, $\overline{\theta}(\lambda_{1l},\lambda_{2m},\lambda_{3n},0) = 0$. Substitution of this solution into the inversion formula (23) gives the final solution in series form.

In Eqs. (22) and (23), when a double integral and its corresponding summation are used (instead of the triple ones), a two-dimensional solutions can be obtained by following the presented procedure.

4. Results and discussions

In this section, the proposed analytical approach is used to investigate the thermal behavior of the sample NiMH battery during fast-charging processes. Solutions for the temperature field inside the battery core, as given in Eq. (23), are obtained and compared to numerical results, and the experimental data from Ref. [21]. To minimize the computational cost, the required calculations can be performed in any software which supports symbolic computation. The authors used MATHEMATICA (Wolfram Research, Inc., Version 8.0) for the analytical calculations and the presented plots. In the following plots, instead of time, SoC is used to present the transient electrical and thermal behavior of the battery. Since capacity of the battery is 30 A h, the charging time at C/2-rate (15 A) and 2C/3-rate (20 A) correspond to 7200 and 5400 s, respectively.

4.1. Model validation with numerical data

The voltage response of the considered NiMH battery during charging processes at 15 A and 20 A is reported in Ref. [21]; shown by symbols in Fig. 3. For each constant-current charging process, polynomials are fitted to the measured values; shown with lines in Fig. 3, and these polynomials are used to evaluate $\dot{g}$ from Eq. (12), see Fig. 4. The linear transformation in (21a) is used to relate the magnitude of $\dot{g}$ to $\dot{G}$, which in our case is $\dot{g} = 2050\dot{G}$.

Due to splitting of the current into charge reaction current and oxygen cycle current [cf. Fig. 2], the rate of heat generation turns out to be a noncontinuous function; solid lines in Fig. 4. In order to facilitate the computations, $\dot{G}$ and $\dot{g}$ are approximated with ninth-order polynomials; dashed lines in Fig. 4. The sharp increase in heat generation for Soc > 75% corresponds to the oxygen recombination heat. Experimental investigations [7,18] confirm such a behavior in NiMH batteries.

Variations of the maximum temperature T_{max} at the center of the battery $\xi = (0.5,0.5,0.5)$ and the minimum temperature T_{min} at the corner of the battery $\xi = (0,0,0)$ as a function of SoC (or time) are shown in Fig. 5. We assume convective heat transfer at all surfaces of the battery case, with small and moderate heat transfer coefficients, $h_{ij,case} = \{6,25\}$, to present cooling effects of natural- and forced-convection with air. Both ambient and initial temperatures are set to $T_0 = 23$ °C. The temperatures T_{max} and T_{min} calculated numerically with a finite element solver (COMSOL Multiphysics, Version 4.2a), shown with symbols, are used to validate the results from the proposed analytical model, shown with lines. In numerical calculation the relative tolerance was set to 10^{-6}. Fig. 5a and b correspond to the battery thermal response at 15 A charging, whereas Fig. 5c and d represent the same information for a 20 A charging current. Two sets of analytical results are shown for T_{max} and T_{min}. The dashed lines denote analytical solution with the first eigenvalue in each direction only, i.e., the first term approximation, and the solid lines present series solutions with multiple eigenvalues, i.e., series solution. The comparisons show a fair agreement between the analytical and numerical results, and as expected, increase in the number of eigenvalues increases the accuracy of analytical solutions at a higher computational cost.

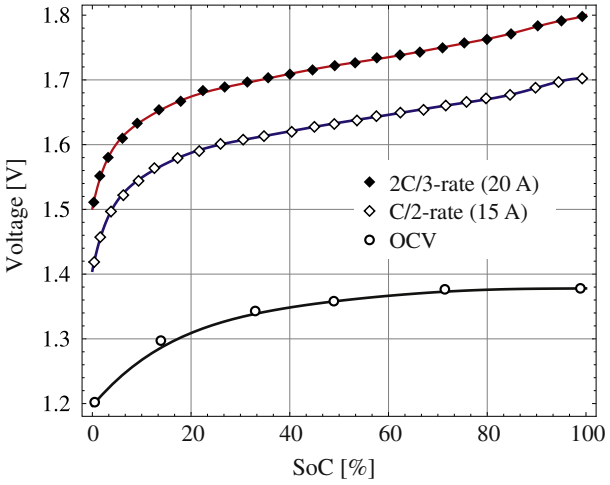

Fig. 3. Variations of the battery voltage versus state-of-charge (SoC) are shown during charging processes. Symbols indicate experimental data [21] for open-circuit voltage (circles), 15 A charging current (white diamonds), and 20 A charging current (black diamonds). Solid lines represent sixth-order polynomial fits to the experimental data.

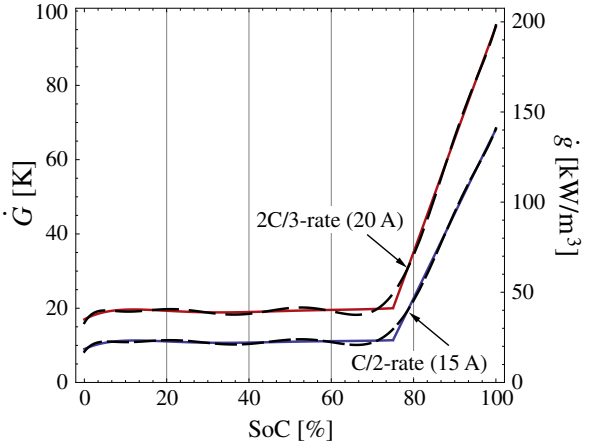

Fig. 4. Variations of heat generation rate $\dot{g}$, and the source for temperature rise $\dot{G}$, versus state-of-charge (SoC) are shown for 15 A and 20 A charging currents. Dashed lines represent ninth-order fitting polynomials.

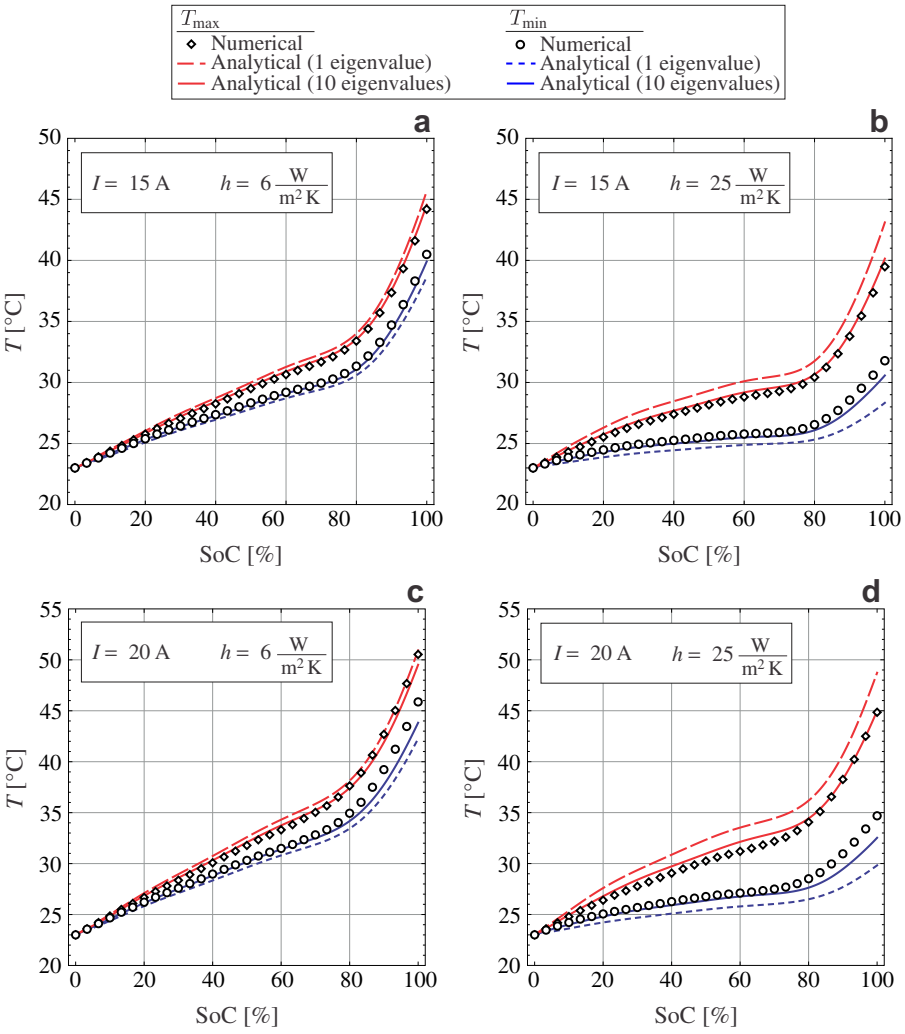

Fig. 5. Temperature variation vs. state-of-charge (SoC) is shown for 15 A charging current (plots a and b) and 20 A charging current (plots c and d). Maximum temperature at the battery center and minimum temperature at the battery corner for $h_{ij,case} = \{6, 25\}$W m^{-2} K^{-1} are compared to numerical data (symbols). Analytical results with first term approximation (dashed lines) and series solution (solid lines) are shown.

4.2. Model validation with experimental data

Fig. 6 compares the calculated (analytical and numerical) temperature profiles and measured temperature values at centerlines of the battery core, along x_1 and x_3 directions, at different charging times with a 15 A charging current under natural convection cooling, $h_{ij} = 6$ W m^{-2} K^{-1}. The experimental temperature data, borrowed from Ref. [21], are measured by K-type thermocouples with an accuracy of ± 1.5 °C.

The comparisons show that the analytical solution with the first term approximation is not very accurate, particularly toward the end of the charging process, i.e., $t = 114$ min. However, an excellent agreement between the analytical and the numerical results can be obtained when multiple eigenvalues (series solution) are used. Indeed, our calculations confirm that for the considered problem, 4 eigenvalues suffice to obtain an accurate analytical solution, and further increase in the number of eigenvalues will not improve the results significantly. Also, the comparison with experimental data reveals that the current splitting scheme and the corresponding heat generation model [cf. Eq. (12)] result in a fair temperature predictions in the thermal model.

The inconsistency between the calculated and measured temperature values at the later times of the charging process are related to the fact that the dependency of heat generation to temperature is neglected in our calculations, since the term $T(dV_{oc}/dT)$ is assumed as a constant. Instead, when a value for dV_{oc}/dT is known, from electrochemical simulations [16,17], and T in the formula for heat generation rate [cf. Eq. (12)] is treated as a variable, then, a better matching with the experimental data is expected. This approach has been recently applied for thermal modeling of Li-ion batteries [20].

Furthermore, the temperature distribution inside the battery strongly depends on the thermal conductivities of the core. In our calculations, thermal conductivities of porous materials in the battery core were approximated by averaging, as given in Eq. (2). In reality, due to the pores distribution and their size, thermal conductivities may vary in different locations. This fact must be addressed as another reason for the differences between the measured and calculated temperature values in Fig. 6.

4.3. Charging efficiency

The fundamental energy balance for the battery states that the total energy E_{tot} provided by the charger splits into electrochemical energy E° stored inside the battery and thermal energy E_{th} which some of it is consumed to increase the battery temperature, and the

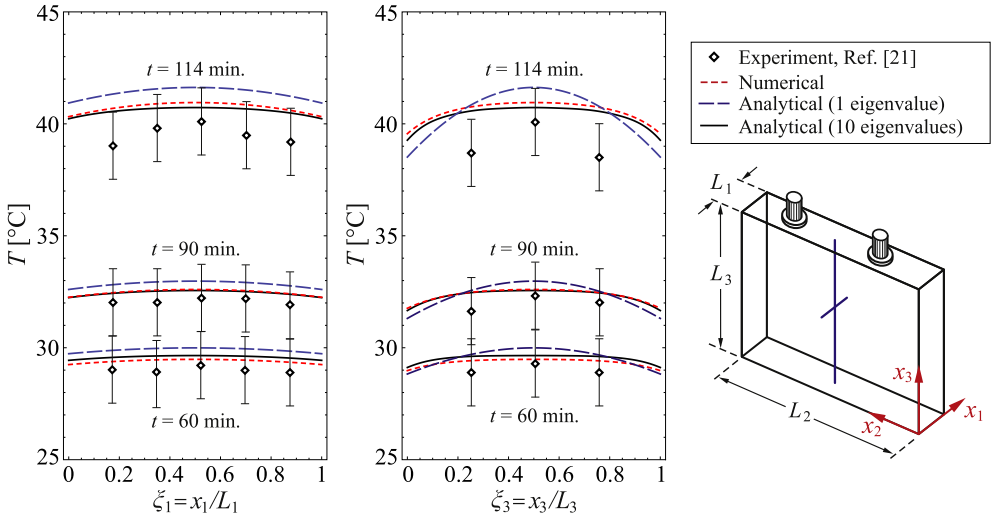

Fig. 6. Calculated temperature profiles at centerlines of the battery core are compared to experimental temperature measurements (symbols) [21]. Numerical results are shown with dashed lines (red) whereas analytical temperature distributions are denoted by long-dashed lines (blue) for first term approximation and solid lines (black) for series solution. Temperature distributions are shown at different times during a charging process at 15 A, subjected to a natural convection cooling, $h_{ij,\mathrm{case}} = 6\ \mathrm{W\ m^{-2}\ K^{-1}}$ at all surfaces of the battery. Ambient and initial temperature of 23 °C was assumed. (For interpretation of the references to color in this figure legend, the reader is referred to the web version of this article.)

rest is dissipated to the surrounding via convection heat transfer. Accordingly, a charging efficiency η can be defined for the battery,

$$\eta = \frac{E^{\circ}}{E_{\mathrm{tot}}} = 1 - \frac{E_{\mathrm{th}}}{E_{\mathrm{tot}}}, \tag{31a}$$

where,

$$E^{\circ} = E_{\mathrm{tot}} - E_{\mathrm{th}}, \quad E_{\mathrm{tot}} = I \int_t V(t)\mathrm{d}t, \quad E_{\mathrm{th}} = \mathscr{V} \int_t \dot{g}(t)\mathrm{d}t. \tag{31b}$$

Based on Eq. (31b), the total energy required for charging the battery at different constant currents can be calculated by integrating the voltage response of the cell, as shown in Fig. 3. Similarly, the thermal energy can be calculated by integrating the heat generation rate inside the cell, as shown in Fig. 4.

Variation of charging efficiency with respect to time is shown in Fig. 7. As expected, charging at the higher rate is less efficient as it yields the higher rate of heat generation [cf. Fig. 4]. Also, the results show that for the considered battery the charging efficiency drops dramatically at high state-of-charge conditions, owing to the initiation of exothermic side reactions. For fast-charging processes at 15 A and 20 A, values of E_{tot}, E_{th}, and E° corresponding to $t = 7200$ s and $t = 5400$ s are listed in Table 3. In both cases, the electrochemical energy E° stored inside the battery is constant, which confirms the battery is equally charged in both charging processes.

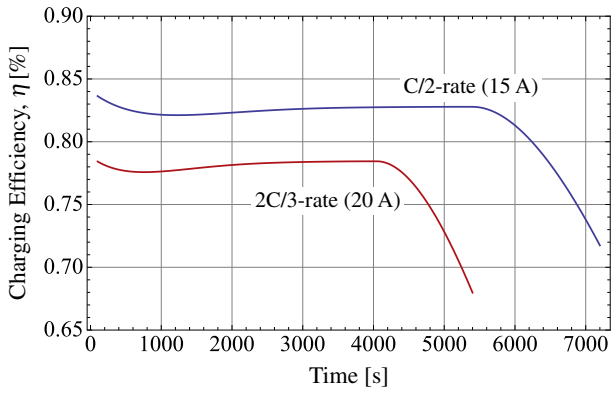

Fig. 7. Variations of the charging efficiency with respect to charging rate and time.

Table 3
Values of total energy, thermal energy, electrochemical energy, and charging efficiency for charging processes at 15 A and 20 A.

Charging current	E_{tot} [J]	E_{th} [J]	E° [J]	η [%]
15 [A]	175 421	49 565	125 856	72
20 [A]	185 141	59 285	125 856	68

From the thermal point of view and the efficiency concerns, results in Figs. 5 and 7 suggest to fast-charge the considered NiMH battery while SoC < 75%, and employ a less aggressive charging profile for the rest of the charging process. This describes why NiMH batteries in hybrid-electric vehicles are preferred to operate in a charge-sustaining mode while the SoC of batteries is maintained below ~75%.

5. Conclusion

Based on the method of integral-transformation, a three-dimensional analytical thermal model is adapted to describe the transient temperature distribution inside the core of prismatic NiMH batteries. The proposed method, which requires the modest numerical effort allows to account for orthotropic heat conduction effects at the presence of transient heat generation and convective heat dissipation.

The proposed thermal model was employed to approximate the thermal response of a 30 A h NiMH cell during fast-charging processes at C/2-rate (15 A) and 2C/3-rate (20 A), where transient heat generation rates were approximated from the electrical performance of the battery.

The accuracy of the model was confirmed through comparison with both numerical and experimental data; thus, it can be

considered as a robust tool for investigating the thermal behavior of batteries in various operating conditions.

The thermal model is used to define a new charging efficiency for batteries, i.e., the ratio of electrochemical energy stored inside the battery to the total energy used for charging the battery, which is an index for describing the percentage of energy wasted as heat.

To conclude, we would like to emphasize on the fact that the presented results were limited to the available experimental data. The presented model is under further development to be coupled with an electrical model for describing current density distribution and the corresponding joule heating effects inside battery electrodes, particularly for high charge/discharge rates. Furthermore, adaptation of the model to large-scale battery assemblies in hybrid and electric vehicle, which experience aggressive transient thermal loads due to the driving cycles, is a straightforward task and is under experimental investigation by the authors.

Acknowledgment

P.T. thanks the guidance of Dr. Mao-Sung Wu (National Kaohsiung University of Applied Science, Taiwan) on the heat generation model. This work was financially supported by Automotive Partnership Canada (APC), Grant No. APCPJ 401826-10.

References

[1] T. Sakai, I. Uehara, H. Ishikawa, J. Alloys Compd. 293–295 (1999) 762–769.
[2] N. Sato, K. Yagi, JSAE Rev. 21 (2000) 205–211.
[3] A. Taniguchi, N. Fujioka, M. Ikoma, A. Ohta, J. Power Sources 100 (2001) 117–124.
[4] D. Berndt, Maintenance-free Batteries: Lead-acid, Nickel/Cadmium, Nickel/Hydride: A Handbook of Battery Technology, Research Studies Press, 1993.
[5] X.G. Yang, B.Y. Liaw, J. Power Sources 101 (2001) 158–166.
[6] J. Shi, F. Wu, D. Hu, S. Chen, L. Mao, G. Wang, J. Power Sources 161 (2006) 693–701.
[7] K.Z. Fang, D.B. Mu, S. Chen, J. Therm. Anal. Calorim. 105 (2011) 383–388.
[8] M.S. Wu, Y.H. Hung, Y.Y. Wang, C.C. Wan, J. Electrochem. Soc. 147 (2000) 930–935.
[9] W.B. Gu, C.Y. Wang, S.M. Li, M.M. Geng, B.Y. Liaw, Electrochim. Acta 44 (1999) 4525–4541.
[10] C. Léger, C. Tessier, M. Ménétrier, C. Denage, C. Delmas, J. Electrochem. Soc. 146 (1999) 924–932.
[11] K.P. Ta, J. Newman, J. Electrochem. Soc. 146 (1999) 2769–2779.
[12] D. Fan, R.E. White, J. Electrochem. Soc. 138 (1991) 2952–2960.
[13] J.W. Weidner, P. Timmerman, J. Electrochem. Soc. 141 (1994) 346–351.
[14] P. De Vidts, R.E. White, J. Electrochem. Soc. 142 (1995) 1509–1519.
[15] S. Motupally, C.C. Streinz, J.W. Weidner, J. Electrochem. Soc. 145 (1998) 29–34.
[16] B. Wu, M. Mohammed, D. Brigham, R. Elder, R. White, J. Power Sources 101 (2001) 149–157.
[17] P.M. Gomadam, J.W. Weidner, R.A. Dougal, R.E. White, J. Power Sources 110 (2002) 267–284.
[18] D. Li, K. Yang, S. Chen, F. Wu, J. Power Sources 184 (2008) 622–626.
[19] J. Shi, F. Wu, S. Chen, C. Zhang, J. Power Sources 157 (2006) 592–599.
[20] P. Taheri, M. Yazdanpour, M. Bahrami, J. Power Sources 243 (2013) 280–289.
[21] M. Wu, Y. Wang, C. Wan, J. Power Sources 74 (1998) 202–210.
[22] J. Kim, T.V. Nguyen, R.E. White, J. Electrochem. Soc. 139 (1992) 2781–2787.
[23] S.C. Chen, C.C. Wan, Y.Y. Wang, J. Power Sources 140 (2005) 111–124.
[24] M.N. Özisik, Boundary Value Problems of Heat Conduction, Dover Publications, New York, 1989.
[25] H.S. Carslaw, J.C. Jaeger, Conduction of Heat in Solids, second ed., Clarendon Press, Oxford, 1959.
[26] J. Newman, K. Thomas-Alyea, Electrochemical Systems, third ed., John Wiley, New Jersey, 2004.
[27] D. Bernardi, E. Pawlikowski, J. Newman, J. Electrochem. Soc. 132 (1985) 5–12.
[28] R. Knödler, J. Appl. Electrochem. 14 (1984) 39–46.

Nomenclature

Bi_{ij}: Biot numbers at surfaces
c_p: heat capacity (J kg^{-1} K^{-1})
E°: electrochemical energy of charging (J)
E_{th}: thermal energy of charging (J)
E_{tot}: total energy of charging (J)
$\dot{g}$: heat generation rate (W m^{-3})
$\dot{G}$: source for temperature rise (K)
$\dot{G}_{irrev}$: irreversible part of $\dot{G}$ (K)
$\dot{G}_{rev}$: reversible part of $\dot{G}$ (K)
h_{ij}: convective heat transfer coefficients at surfaces (W m^{-2} K^{-1})
I: total charge/discharge current (A)
I_1: current of charging reaction (A)
I_2: current of oxygen cycle reaction (A)
K_i: dimensionless thermal conductivity in x_i direction
ℓ: thickness (m)
L_i: dimension of battery core in x_i direction (m)
m: mass (kg)
N: number of layers in battery core
Q: nominal battery capacity (A h)
R_z: apparent DC resistance of battery (Ω)
t: time (s)
T: core temperature (K)
T_0: ambient and initial temperatures (K)
T_{ij}: surface temperatures (K)
V: operational battery voltage (V)
V_{oc}: open circuit potential (V)
$\mathscr{V}$: volume of battery core (m^3)
x_i: position in Cartesian coordinate system (m)
ARC: accelerating rate calorimeter
Li-ion: lithium-ion
NiMH: nickel–metal hydride
OCV: open circuit voltage
SoC: state-of-charge

Greek
α_i: normalization factors for eigenfunctions in x_i direction
ε: porosity
η: charging efficiency
θ: core temperature rise (K)
θ_{ij}: temperature rise at surfaces (K)
κ_i: thermal conductivity in x_i direction (W m^{-1} K^{-1})
λ_i: eigenvalues in x_i direction
ξ_i: dimensionless position in Cartesian coordinate system
ρ: mass density (kg m^{-3})
τ: dimensionless time
ϕ: eigenfunction
ψ: transformation kernel

Sub-/super-script
case: related to battery case
f: related to filler (liquid) structural material
m: related to membrane
n: related to negative electrode
p: related to positive electrode
s: related to solid structural material
$\bar{}$: transformed quantity based on Eq. (22)